Academic Journal of Science and Technology
ISSN: 2771-3032 | Vol. 14, No. 2, 2025

Well-to-Ground Electrical Resistivity Tomography (ERT) for Fracture Monitoring in Shale Gas Reservoirs: Application to the Wulalike Formation

Cixun Wang[1], Hui Zhao[2] and Fei Xie[1]

[1]School of Earth Sciences and Engineering, Xi'an Shiyou University, Xi'an 710065, China
[2]School of Petroleum Engineering, Xi'an Petroleum University, Xi'an 710065, China

Abstract: Advancing deep-seated geological exploration represents a strategic scientific and technological imperative. Reservoir modification through hydraulic fracturing constitutes an indispensable component of deep oil and gas development, where precise fracture monitoring and evaluation in deep gas reservoirs serve as critical technical safeguards for technological innovation. To address the need for real-time monitoring of fracture length and width in the horizontal well Z2 of Wulalike Formation in Yanchuan Basin, this study employs Well-to-Ground Electrical Resistivity Tomography (ERT) technology. By leveraging the electrochemical property contrasts between pre- and post-fracturing fluids in target zones, we integrate control volume method-based resistivity forward modeling with nonlinear least squares inversion algorithms to analyze subsurface electrical field variations within a 1000-meter radius around the 4000-meter depth level in the horizontal section of Z2 well. Field implementation demonstrates that Well-to-Ground ERT provides an effective methodology for real-time fracture monitoring in deep horizontal shale gas wells with centimeter-scale resolution.

Keywords: Well-to-ground ERT exploration; Control volume method; Gas reservoir; Hydraulic fracturing; Fracture monitoring.

1. Introduction

The current widely adopted technical methods for in-situ hydraulic fracturing fracture monitoring include microseismic monitoring, tracer monitoring, and distributed fiber-optic acoustic sensing (DAS). Microseismic monitoring techniques can dynamically track the fracturing process in real time. Yang Yongyu et al. [1] applied microseismic fracture monitoring to three coalbed methane wells in Liupanshui, obtaining geometric parameters such as fracture network distribution and extension direction, and comprehensively analyzed reservoir modification effects during and after fracturing. Shen Baojian et al. [2] used tracer technology to evaluate the connectivity of Fuling shale gas reservoirs, demonstrating the feasibility of developing Jiao Ye 66-Z2HF well. Their research verified that tracer methods can efficiently and conveniently assess shale gas well connectivity, though potential issues with stratum contamination remain.

Distributed fiber-optic monitoring systems mainly include acoustic sensing (DAS) and temperature sensing (DTS). DAS technology employs fiber-optic sensors deployed along the wellbore to capture full-borehole, wide-azimuth, high-density real-time micro-vibration data, providing richer information for microseismic analysis and fluid studies [3].

In-ground ERT exploration technology uses high-density transmitter and receiver systems to perform electrical field tomography, imaging resistivity variations by exploiting differences in target layer resistivity relative to surrounding rocks and strata. This technology has been tested in oil reservoir pre-exploration in China's Liaohua and Turpan regions with positive results [4], but its application in gas reservoir fracturing monitoring remains limited. To overcome the adverse effects of loess layers, this study implemented measures including increased transmission current, enhanced reception sensitivity, optimized monitoring center selection, and multi-channel measurement methods to strengthen signal penetration capacity, achieving significant monitoring effectiveness.

2. Well-to-Ground Potential Method Monitoring Technology Principle

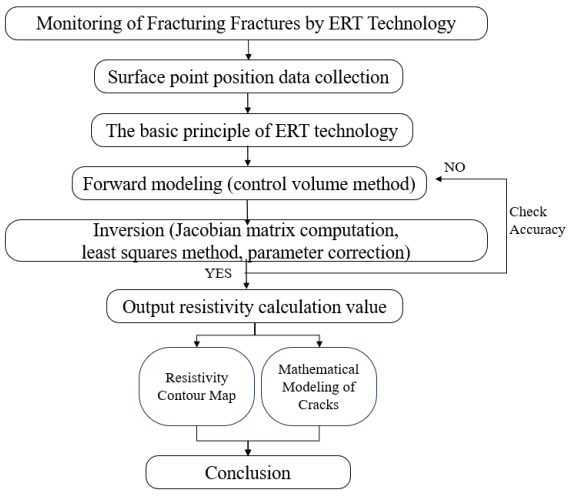

Figure 1. Fracturing fracture monitoring technology roadmap of ERT technology

The theoretical framework of well-to-ground ERT exploration comprises forward theory and inverse theory, with detection methods encompassing the observation system, field implementation procedures, and corresponding data processing/interpretation approaches. Forward theory calculates the distribution of earth currents and electric fields based on a predefined observation system and subsurface

resistivity distribution, while inverse theory reconstructs a three-dimensional resistivity distribution of the subsurface by inverting surface electric field measurements obtained via the observation system [5].

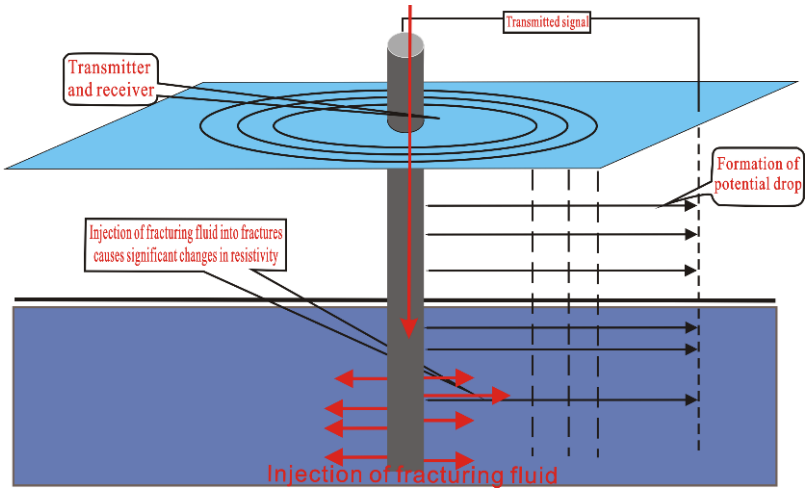

Figure 2. The schematic diagram of ERT technology monitoring

2.1. Principle of Forward Calculation

$$\begin{cases} \nabla \cdot (\sigma \nabla v) - k^2 \sigma v = -I\delta(A), \in \Omega \\ \dfrac{\partial v}{\partial n} = 0, \in \Gamma_s \\ \dfrac{\partial v}{\partial n} + k\dfrac{K_1(kr)\cos(r,n)}{K_0(kr)} v = 0, \in \Gamma_\infty \end{cases} \quad (1)$$

In the equation, ∇ is the two-dimensional Hamiltonian operator; k is Fourier-domain wave number; A is a point source; Γ_s and Γ_∞ denote the surface and infinite underground boundaries of the study area Ω .; n is the outward normal direction of the underground infinite boundary; r is the distance from the point current source A to the boundary; I is injected current; K is Modified Bessel Function.

In Figure 3, the dark area represents the control volume of node P., In the figure, w, n, e, s represent the control boundaries, while W, N, E, S are the adjacent nodes of node P. The distances from node P to nodes W, N, E, and S are denoted as δx_{WP} 、 δz_{PN} 、 δx_{PE} 、 δz_{SP} .

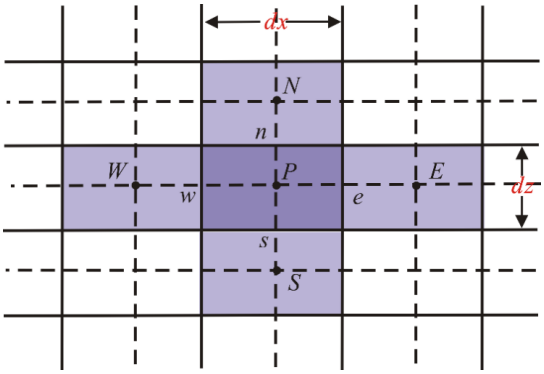

Figure 3. Two-dimensional grid system of volume

By applying the control volume method, the volume integral of Equation (1) is performed to obtain the conservation equation:

$$\int_{\Delta V} \nabla \bullet (\sigma \nabla U) dxdz - \int_{\Delta V} k^2 \sigma U dxdz = -\int_{\Delta V} I\delta(A) dxdz \quad (2)$$

By integrating the governing equations satisfied by all nodes and incorporating boundary constraints for the boundary nodes using Equation (1), the global finite volume linear equation system can be derived as follows:

$$a_P v_P = a_W v_W + a_E v_E + a_S v_S + a_N v_N + S_v \quad (3)$$

Within the theoretical framework of computational mathematics, the method of weighted residuals encompasses a variety of strategies, including the control volume method, finite element method, and finite difference method. Among these, the control volume method stands out due to its intuitive theoretical foundation and clear physical interpretation, which facilitate the derivation of governing equations. This method significantly reduces storage requirements during computation and effortlessly addresses the challenges of three-dimensional applications. Compared to the finite difference method, the control volume method demonstrates superior numerical stability, particularly when tackling problems with strong nonlinear characteristics. Even under conditions of coarse grid resolution, the control volume method is capable of effectively approximating physically realistic solutions.

The core advantage of the control volume method lies in its solution accuracy. Integral conservation of physical quantities such as mass, momentum, and energy is precisely satisfied, both within individual control volumes and across the entire computational domain. This characteristic ensures that the method maintains integral conservation of physical quantities across any number of grid nodes. Even with coarse grids, the system can accurately preserve integral balance. Such high levels of precision and stability have established the control volume method as a prominent approach in the field of computational mathematics [6].

2.2. Principles of Inverse Calculation

Most geophysical inversion problems exhibit nonlinear characteristics. When inverting underground resistivity parameters from field data, nonlinear least squares methods are typically employed for computation. The results are obtained by iteratively calculating the correction values of the parameters.

$$(A^{T}A + \lambda C^{T}C)\Delta P = A^{T}\Delta g \quad (4)$$

Here, A is the Jacobian matrix, λ is the damping factor, C is the smoothing filter, ΔP is the parameter correction vector, and Δg is the residual vector. The inversion process proceeds according to the following steps: First, forward modeling is performed, and the measured values are compared with the calculated values to obtain the residuals. Next, the Jacobian matrix is computed. Then, the linear least squares equation is solved to determine the parameter corrections. Finally, if the residuals between the measured and calculated values do not meet the accuracy requirements, the steps of forward modeling and Jacobian matrix computation are repeated [7].

2. Basic Monitoring Situation of Well Z2 Fracturing

Well Z2 is a pre-exploratory well located in the Tianhuan Depression of the Ordos Basin. The well has a total drilled depth of 5,300 meters (measured depth) / 4,205.4 meters (true vertical depth), with the target entry point at 4,640 meters. The horizontal section of the well is 660 meters long, with a bottomhole azimuth of 135.74° and a bottomhole displacement of 1,324.01 meters. The well was completed in the Wulalike Formation, which is also the target formation. The lithology of the horizontal section consists of light yellowish-gray gas-bearing siliceous shale, dark gray gas-bearing calcareous mudstone, and white-brown argillaceous limestone.

The horizontal section was initially planned to be fractured in 8 stages. However, due to operational complexities, particularly the high treatment pressure and difficulties in fracture initiation and propagation encountered in the first stage, the fracturing parameters for the entire well section were optimized in four key aspects: perforation technology, number of clusters per stage, slickwater application, and pre-pad acid volume. As a result, the actual fracturing operation was conducted in 7 stages with 18 clusters.

The operation involved a total of 341 cubic meters of proppant, 11,930.3 cubic meters of fluid, and 282 cubic meters of acid. The injection rate ranged from 11 to 16 cubic meters per minute, with a proppant concentration of 8-10%. The treatment pressure varied between 75 and 107 MPa.

The casing of Well Z2 was utilized as the current source electrode (A electrode), with the midpoint of the 5th fracturing stage serving as the detection center (M point). The return electrode (B electrode) was positioned on the surface, located 8,000 meters away from the detection center (M point) along the extension direction of the horizontal section (121°). A radial monitoring system was employed, with survey lines spaced at 20° intervals. A total of 18 radial survey lines were arranged around the well, each containing 20 observation points spaced 50 meters apart. Within a 1,000-meter radius centered at the M point, 360 ground electric field receivers were deployed.

Inversion was performed for the intervals of 4,203–4,205 meters and 4,205–4,215 meters to obtain the resistivity distribution map, which served as a reference for post-fracturing resistivity anomalies. In Figure 4, the blue dots represent different fracturing stages, and the red dashed line indicates the horizontal projection of the well trajectory.

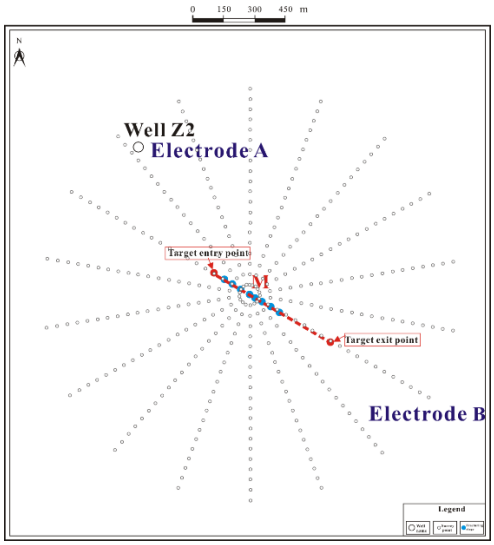

Figure 4. Distribution diagram of fracture monitoring in well Z2

3. Application Example of Well-Surface Potential Method Monitoring

The principle of using well-surface Electrical Resistivity Tomography (ERT) technology to monitor hydraulic fracturing is based on the difference in resistivity between the formation and the fractures filled with fracturing fluid after the fracturing operation. By collecting surface potential data at fixed points and processing it through computer algorithms, the lateral potential contour map of the electric field distribution is generated via inversion calculations. Utilizing the principle of spatial electric field superposition and specialized fracturing fracture interpretation software, the data is processed and interpreted to obtain parameters such as the length, width, and affected area of the fractures. By combining resistivity anomaly regions at two different depths, the distribution of the fracturing fractures can be predicted.

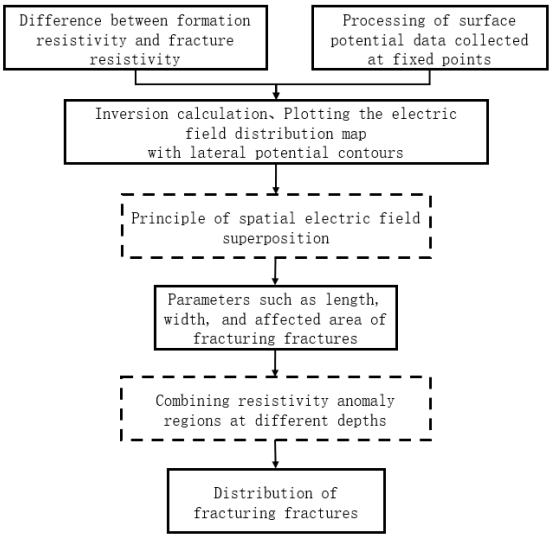

Figure 5. Application flow chart of ERT technology in Wells

3.1. Comparison of Resistivity Anomalies Before and After Fracturing

Figures 6 and 7 show the resistivity maps of the target layer (4,203.0–4,205.0 meters) before and after fracturing. The interpretation indicates that the resistivity of the target layer is greater than 22.56 Ω·m. In Figure 7, segments 1-1 to 7-2 represent the actual fracturing stages. Areas with resistivity less than 22.56 Ω·m are identified as regions invaded by fracturing fluid, resulting in a reduction in original resistivity, which corresponds to fracture development zones.Low-resistivity anomalies are primarily distributed across 10 clusters: 1-1, 1-2, 1-3, 1-4, 2-1, 4-1, 4-2, 5-1, 5-2, and 5-3. The remaining 8 clusters—2-2, 3-1, 3-2, 6-1, 6-2, 6-3, 7-1, and 7-2—show no significant low-resistivity anomalies in the interval of 4,203.3–4,205.0 meters.

The pre-fracturing resistivity map indicates the presence of an original low-resistivity zone at 146 meters in the 225° direction within Stage 1. Post-fracturing, the resistivity anomaly map for this stage shows a low-resistivity anomaly at 107 meters in the 225° direction, which should correspond to the original low-resistivity zone of the formation. (In the figure, the fracturing segments from 7-n to 1-n are represented by colored short lines sequentially along the 135° direction.)

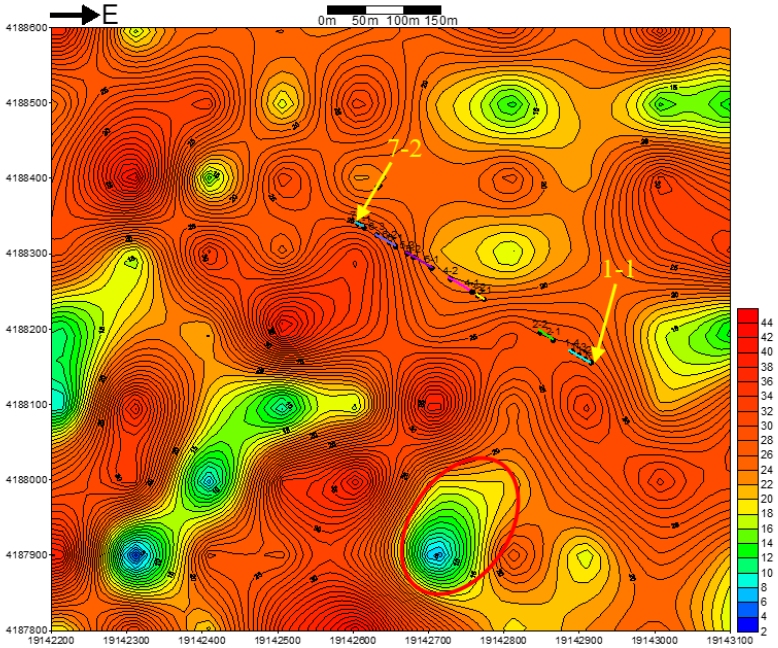

Figure 6. Resistivity plan of well Z2 before fracturing (4203.0-4205.0m)

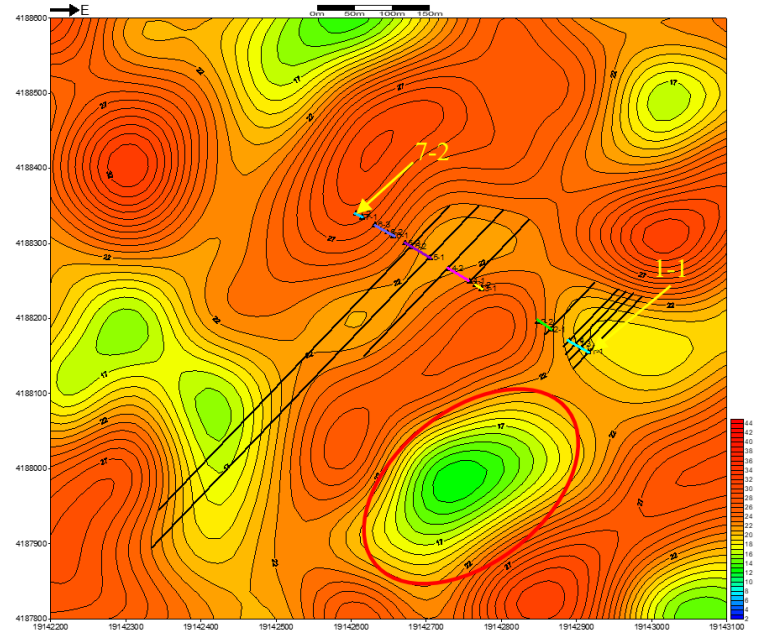

Figure 7. Post-Fracturing Resistivity Planar Map of Well Z2 (4203.0-4205.0m)

Figures 8 and 9: Resistivity Maps Before and After Fracturing for the Target Interval (4,205.0–4,215.0 meters) , Figures 8 and 9 present the resistivity maps of the target interval (4,205.0–4,215.0 meters) before and after fracturing. The interpretation indicates that the resistivity of this interval is ≥22.5 Ω·m. In Figure 9, segments 1-1 to 7-2 represent the actual fracturing stages. Areas with resistivity less than 22.5 Ω·m are identified as regions invaded by fracturing fluid, resulting in a reduction in the original resistivity, which corresponds to fracture development zones.Low-resistivity

anomalies are primarily distributed across 12 clusters: 1-2, 1-3, 1-4, 2-1, 2-2, 5-2, 5-3, 6-1, 6-2, 6-3, 7-1, and 7-2. The remaining 6 clusters—1-1, 3-1, 3-2, 4-1, 4-2, and 5-1—show no significant low-resistivity anomalies in the interval of 4,205.0–4,215.0 meters.

The pre-fracturing resistivity map indicates the presence of an original low-resistivity zone at 50 meters in the 225° direction within Stage 1. Post-fracturing, the resistivity anomaly map for this stage shows a low-resistivity anomaly at 157 meters in the 225° direction, which should correspond to the original low-resistivity zone of the formation. (In the figure, the fracturing segments from 7-n to 1-n are represented by colored short lines sequentially along the 135° direction.)

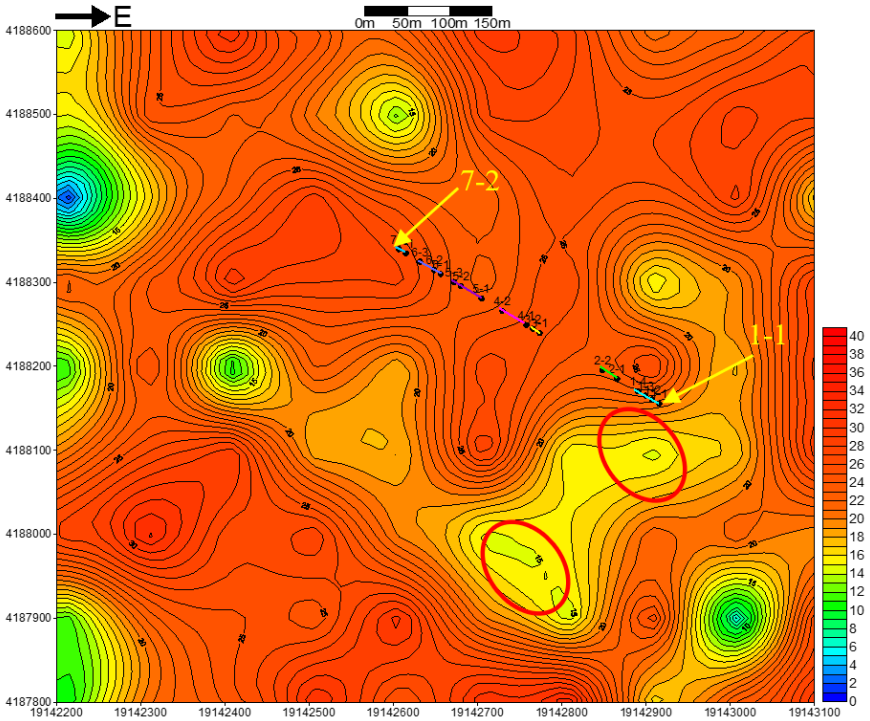

Figure 8. Resistivity plan of well Z2 before fracturing (4205.0m~4215.0m)

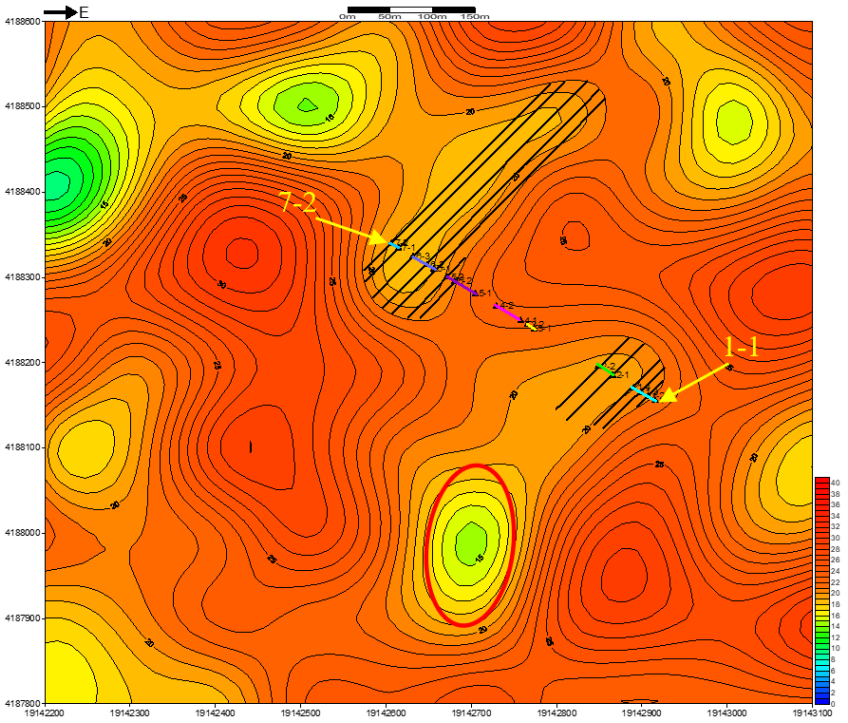

Figure 9. Post-Fracturing Resistivity Planar Map of Well Z2 (4205.0m~4215.0m)

3.2. Monitoring Results

The invasion of fracturing fluid into the formation results in a reduction of the original resistivity, indicating fracture development zones. Based on the changes in resistivity before and after fracturing in the depth intervals of 4,203.0–4,205.0 meters and 4,205.0–4,215.0 meters, inversion calculations and numerical simulations were performed for anomalies at different depths. This allowed for the creation of the fracture distribution map (Figure 10) and the fracture simulation map

(Figure 11) for Well Z2.

In this study, fractures in different directions exhibited varying lengths and widths. In the 45° direction, the shortest fracture length was observed in Stage 3, measuring only 49 meters, while the longest fracture length was observed in Stage 6, reaching 291 meters. In the 225° direction, the shortest fracture length was observed in Stage 7, measuring only 57 meters, while the longest fracture length was observed in Stage 5, reaching 537 meters. Additionally, the minimum fracture width was observed in Stage 7, measuring only 18.1 meters, while the maximum fracture width was observed in Stage 5, reaching 50.1 meters. In terms of fracture area, the smallest affected area was observed in Stage 2, measuring only 2,737 m², while the largest affected area was observed in Stage 5, reaching 20,959 m².

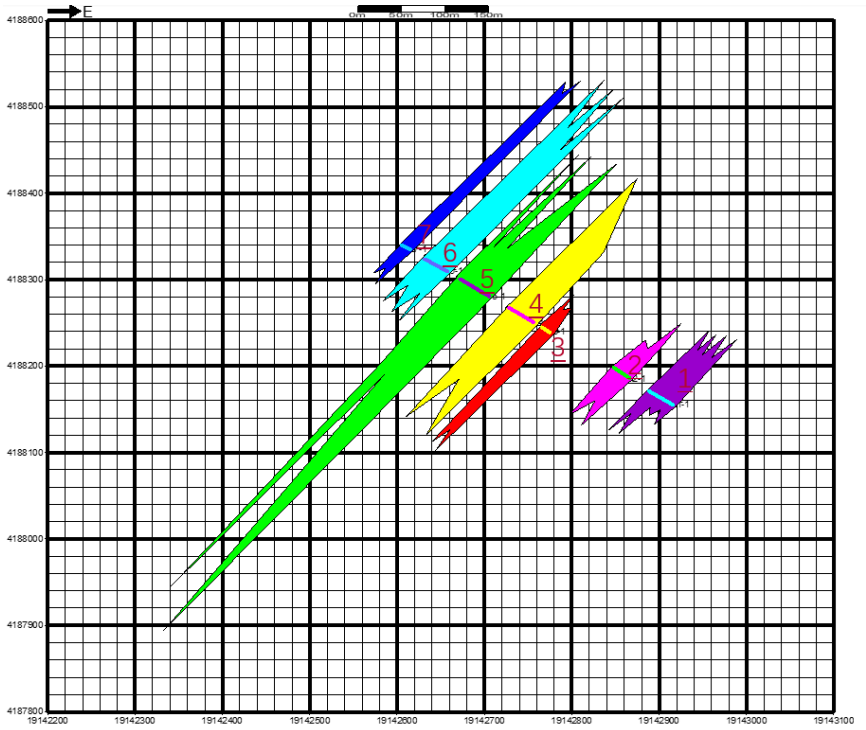

Figure 10. Fracture distribution pattern plan of well Z2

Using the actual resistivity value of the fracturing fluid as a reference, resistivity values with residuals meeting the accuracy requirements were selected for three-dimensional digital modeling. As shown in Figure 11, the dark blue regions represent the volume morphology of the fracturing fluid when it fully fills the fractures, while the yellow regions represent the trajectory of the horizontal well section. This indirectly reflects the three-dimensional morphology of the fracturing fractures.

From Figure 11, it can be observed that:

Stages 7 and 6 exhibit "X"-shaped fractures in the 225° direction.

Stages 5, 4, and 3 show clustered planar fractures in the 225° direction.

Stages 2 and 1 display radial fracture patterns in the 45° direction.

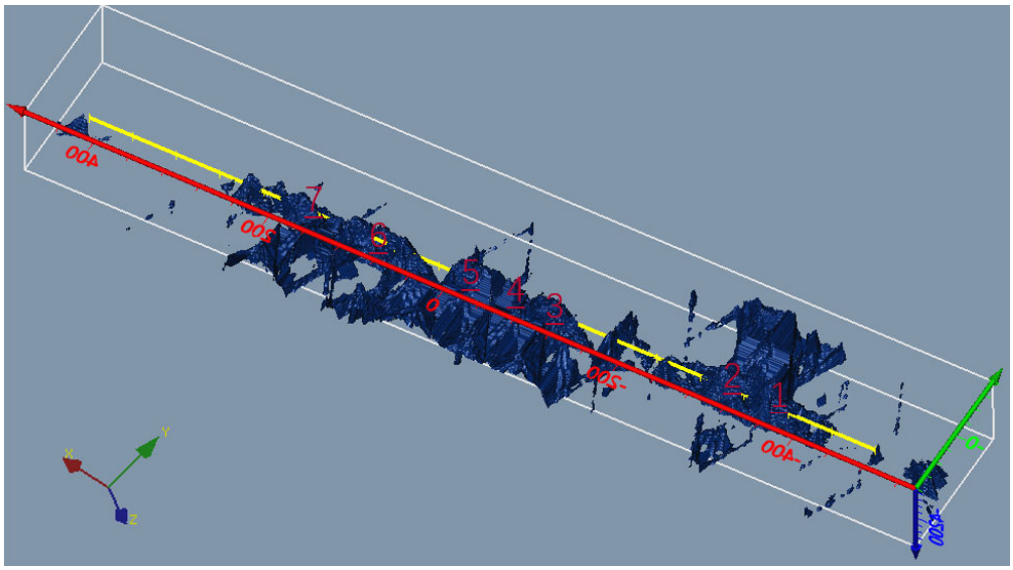

Figure 11. 3D Representation of Fracture Geometry in Hydraulic Fracturing of Z2 Well.

3.3. Comprehensive Analysis and Comparison

3.3.1. Analysis of Construction Parameters and Fracturing Parameters

Table 1. Statistical table of fracture spread in well Z2

Fracturing Stage	Total Fluid Volume/m^3	Proppant Volume /t	Injection Rate m^3/min	Direction	Length /m	Width /m	Affected Area /m^2
1 paragraph	1368.6	14	11.0-14.0	45° 225°	107 64	44.0	4259
2 paragraph	1628.2	73	14.0-16.0	45° 225°	87 77	30.3	2737
3 paragraph	1355.6	60	14.0-16.0	45° 225°	49 191	21.0	3037
4 paragraph	1159.0	26	15.0-16.0	45° 225°	202 177	43.3	11288
5 paragraph	1855.2	80	15.0-16.0	45° 225°	208 537	50.1	20959
6 paragraph	1570.7	46	14.0-16.0	45° 225°	291 81	36.0	10027
7 paragraph	1430.1	42	13.0-15.0	45° 225°	278 57	18.1	4582

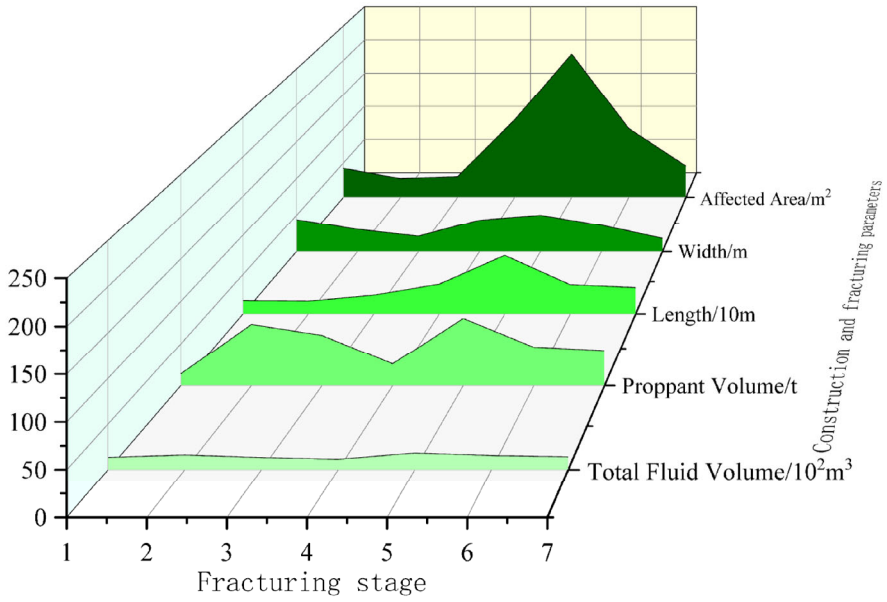

Figure 12. Trend chart of parameter variations

From Figure 12, it can be observed that the trends of construction parameters (total fluid volume, proppant volume) and fracturing parameters (total fracture length, width, and affected area) exhibit a certain degree of correlation. Particularly in Stage 5, the total fluid volume, proppant volume, fracture length, width, and affected area all reach their peak values, further validating the reliability of the monitoring results.

3.3.2. Analysis of Fracturing Operation Curves

The study (Figure 13) reveals that as the injection rate increases, the formation is filled with fracturing fluid, causing the pressure to gradually rise. At a certain point, when the formation is fractured to create new fractures or connect with natural fractures, the pressure drops significantly. The third, fifth, sixth, and seventh stages exhibit a characteristic curve where the surface pressure sharply increases and then slowly decreases, corresponding to the unidirectional fracturing advantage in the 45° or 225° direction as shown in Table 1. Taking the fifth stage as an example, a comprehensive analysis (Figures 10 and 11) indicates that the dominant fracturing direction is 225°. When fracturing reaches approximately 200 meters and encounters the original low-resistivity formation, natural fractures are connected, resulting in the maximum fracture length and affected area for the fifth stage.

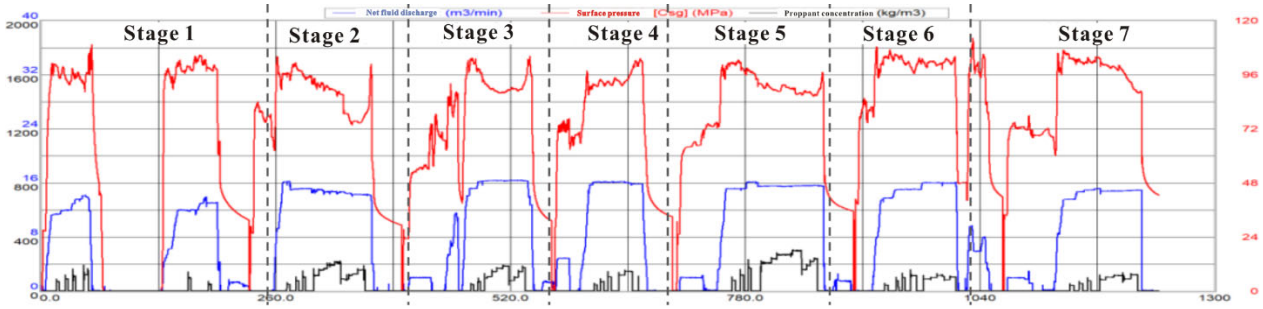

Figure 13. Construction curve of section 1-7 of well Z2

3.3.3. Analysis of Production Performance Curves

The production performance curve is the most critical indicator for evaluating the effectiveness of fracturing. Based on the analysis of production data from Well Z2 over one year (Figure 14), the initial monthly gas production after fracturing was approximately 100,000 cubic meters, followed by a gradual decline and eventual stabilization. After the fracturing operation, the monthly gas production stabilized at around 200,000 cubic meters. The gas production from Well Z2 remained relatively stable post-fracturing. In the first eight months after fracturing, the cumulative gas production was approximately 900,000 cubic meters, while in the subsequent eight months, it reached about 2.38 million cubic meters. From the perspective of hydrocarbon recovery efficiency, the fracturing operation achieved excellent results.

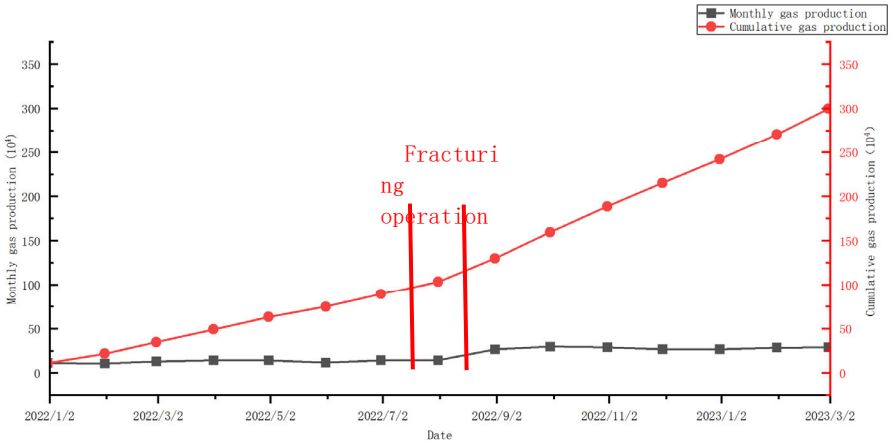

Figure 14. Production data curve of horizontal well Z2

4. Summary

The well-surface ERT (Electrical Resistivity Tomography) technology utilizes single-well tomography inversion to calculate the resistivity changes in the target formation. By analyzing the relationship between the resistivity of the target formation before and after the injection of fracturing fluid into the fractures, the distribution direction of the fracturing fractures can be determined.

1.Fracturing Design and Implementation:

Originally, Well Z2 was planned to be fractured in 8 stages, but only 7 stages were actually fractured during implementation. A reasonable data acquisition scheme was designed and executed to perform resistivity stratification analysis on the horizontal section of Well Z2. This allowed for the determination of fracture length, width, and affected area.

2. Optimal Fracturing Design:

The design of the horizontal section casing in Well Z2, which was perpendicular to the fracturing direction, achieved relatively ideal fracturing results. This design provides a reference for post-fracturing evaluation.

Practice has proven that the well-surface ERT technology can serve as an effective method for monitoring fracturing fractures in deep gas reservoirs, even when the surface terrain is complex, such as in loess plateau regions.

References

[1] Xing, C., Luo, Y. P., Guo, X. J., et al. Simulation Analysis of Monitoring Effect of Resistivity Tomography in Seawater-Groundwater Exchange Process[J]. Progress in Geophysics, 2022, 37(06): 2622-2629.

[2] Zhou, Z. H., Du, Y. J., Yao, W., et al. Application of Electrical Resistance Tomography Technology in Monitoring the Cavity Shape of Salt Cavern Gas Storage[C]//Proceedings of the 33rd National Natural Gas Academic Annual Conference (2023) (01 Geological Exploration), 2023.

[3] Zhao, J. H., Liu, C. L., Zou, C. C., et al. Visual Detection Simulation Experiment of Hydrate-Bearing Sediments Based on ERT Technology[J]. Marine Geology & Quaternary Geology, 2021, 41(06): 206-212.

[4] Liu, H. Z., Liu, Z. D., Liang, W. J., et al. Analysis of the Application Effect of Downhole Microseismic Monitoring Technology—Taking Zhuang 288 Block as an Example[J]. Journal of Hebei GEO University, 2021, 44(04): 50-55.

[5] Yang, Z. Y. Functional Improvement Design of ERT System[D]. Jilin University, 2016.

[6] Liu, Q. H. Data Processing, Inversion and Interpretation of Well-Field ERT Water Drive Front[D]. Jilin University, 2015.

[7] Wang, X. Z. Application of Well-Field Potential Method in Fracture Monitoring of CBM Wells[J]. Coal Engineering, 2006,(05): 36-37.

[8] Song, R. C. Research on Cross-Borehole Resistivity Tomography of Bedrock Water-Conducting Fracture Zone[D]. Shandong University, 2021.

[9] Liu, Y. M. Three-Dimensional Imaging Method of Multiple Resistivity Data Fusion and Its Engineering Application[D]. Shandong University, 2021.

[10] Li, Z. T. Three-Dimensional Resistivity Inversion Imaging Technology for Reservoirs and Its Application in Residual Oil Detection[D]. China University of Geosciences (Beijing), 2005.

[11] Liu, P. Research and Application of Time-Lapse Resistivity Tomography[D]. China University of Mining and Technology. 2008, Vol. 42 (No. 11), p. 231-236.